Electronic Supplementary Information

Dynamic light scattering analysis of size-selected graphene oxide 2D colloids fractioned via liquid crystal phase separation

Christina D. Abele[a] and Frank Giesselmann *[a]

[a]*Institute of Physical Chemistry, University of Stuttgart., Pfaffenwaldring 55, 70569 Stuttgart, Germany*

ESI 1: UV/VIS spectroscopy

The absorbance of GO dispersions varies strongly with the GO mass fraction according to Lambert-Beer law, since the GO sheets absorb in the UV region. With absorbance measurements the GO mass fraction can be determined. A calibration line (Fig. S1) was obtained for different GO mass fractions ranging from 0-0.4 wt%. With that, the sample mass fractions of the fractions obtained with the size fractionation protocol were calculated. This method was used to determine the GO content instead of a gravimetric method because the overall GO mass fraction of the fractions is low and a large sample quantity would have been required. To note is, that there is a small change of the absorbance with the GO sheet size, due to the change of chemical composition of the functional groups during size reduction by sonication. But this is negligible compared to the strongly varying absorbance with the GO mass fraction.

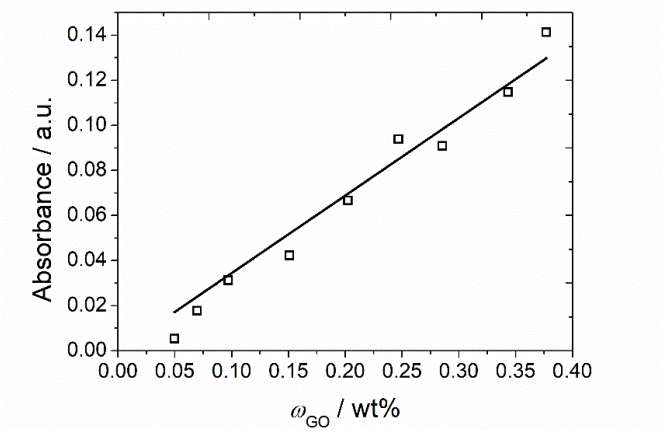

Fig. S1: Absorbance at λ_0 = 430 nm of several dispersions with different GO mass fractions ω_{GO}, measured in 0.4 mm thick rectangular capillaries. The data points are fitted with a line (slope: 0.344 wt%$^{-1}$), which is used as calibration line to determine the GO mass fraction from the absorbance of an unknown samples.

ESI 2: Polarized DLS measurements of the sonication series

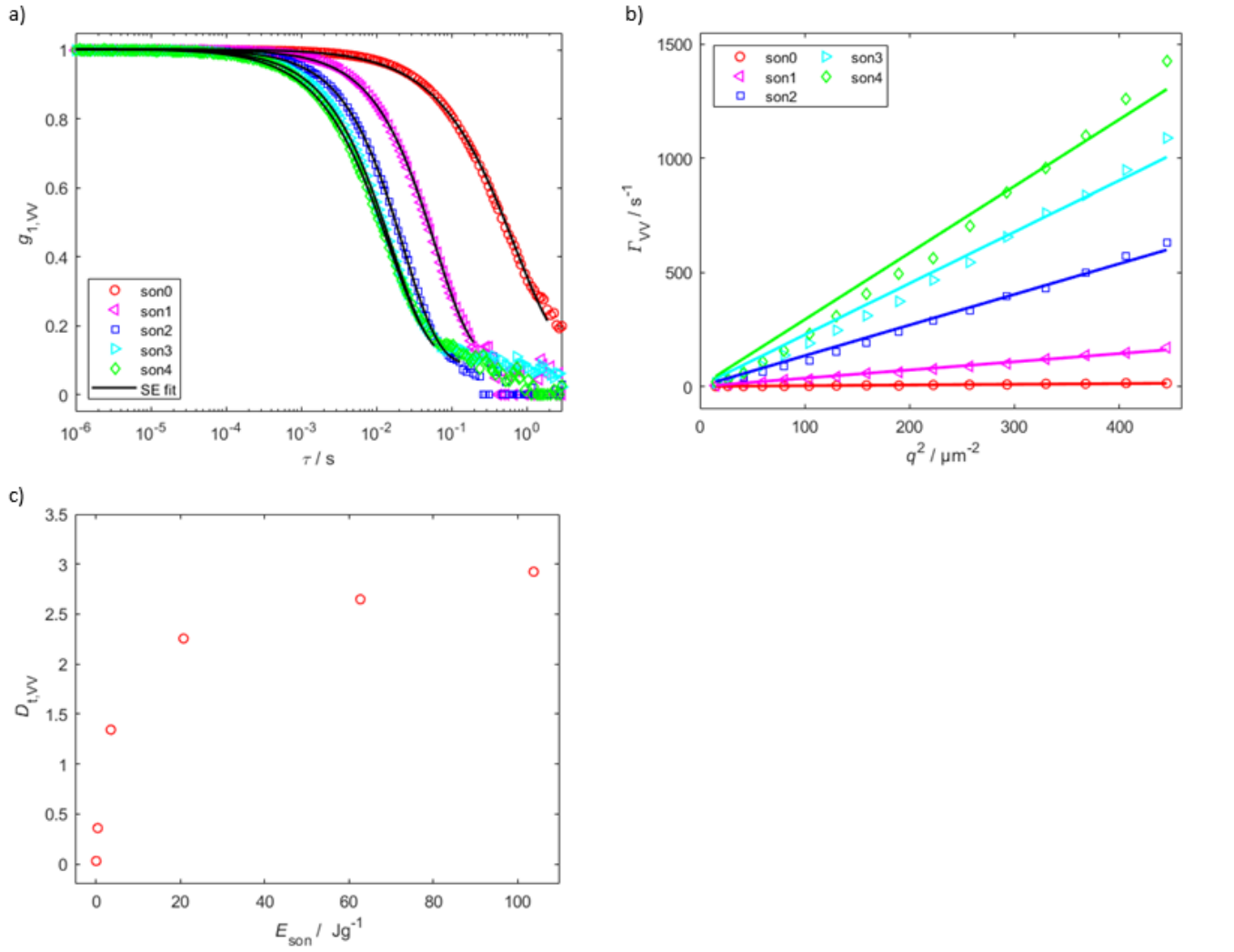

Fig. S2: DLS measurement of the sonication series, measured in polarized geometry. GO samples with different sheet size, which were obtained by different sonication energy densities (son0: no sonication, son1: 0.37 Jg^{-1}, son2: 3.47 Jg^{-1}, son3: 20.74 Jg^{-1} and son4: 103.82 Jg^{-1} were compared. a) **A**mplitude correlation functions $g_{1,VV}$ and stretched single exponential (SE) fit at a scattering vector of q = 6.46 µm^{-1}. b) Mean inverse relaxation time Γ_{VV} and c) translational diffusion coefficient $D_{t,VV}$ for different sonication energies. The same trends regarding the correlation functions, the inverse relaxation times and the diffusion coefficients were observed as for the depolarized DLS measurements.

ESI 3: Stretching exponents

The stretching exponents were obtained from the fits of $g_{1,i}(q,t)$ $(i = VH,VV)$ according to equation (2) for the samples of the sonication series. The size polydispersity is related to the stretching exponent. The values of β_i were low for all samples of the sonication series, indicating a high polydispersity for all of these samples. Further, a dependence of β_i with q was observed, which has minor influence on the inverse relaxation rate Γ_i and the particle size, because the stretching is considered by the calculation of Γ_i, as shown in equation (3).

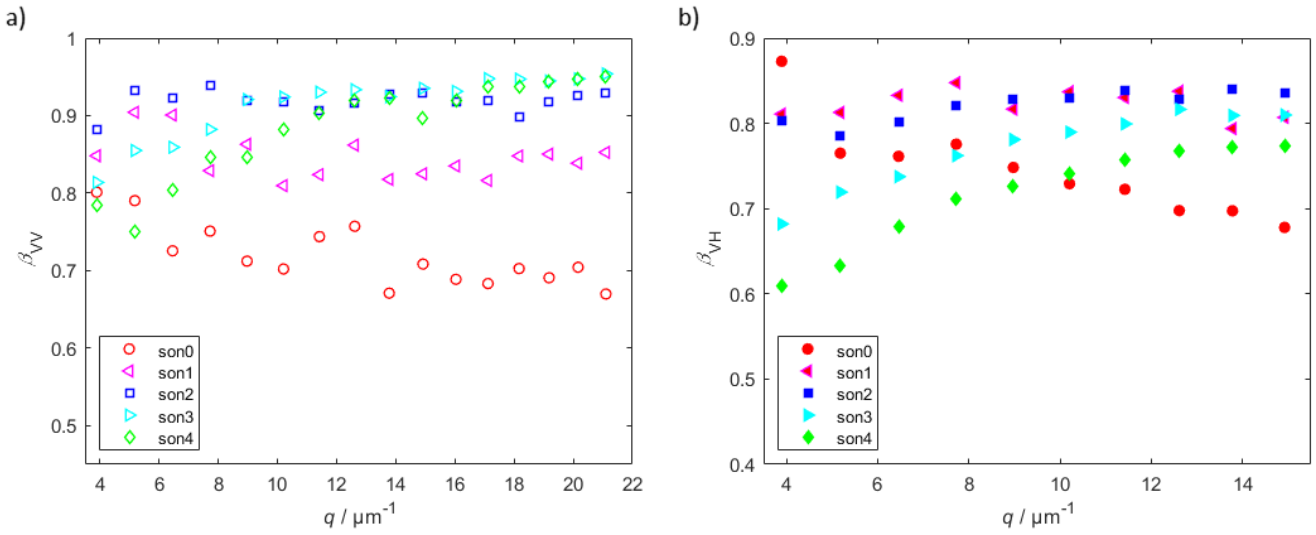

Fig. S3: Evolution of the stretching exponent a) β_{VV} in polarized (VV) and b) β_{VH} in depolarized (VH) scattering geometry for different scattering vectors q and different GO samples with different sheet size, which were obtained by different sonication energy densities (son0: no sonication, son1: 0.37 Jg^{-1}, son2: 3.47 Jg^{-1}, son3: 20.74 Jg^{-1} and son4: 103.82 Jg^{-1}.

ESI 4: Transmission electron microscopy (TEM)

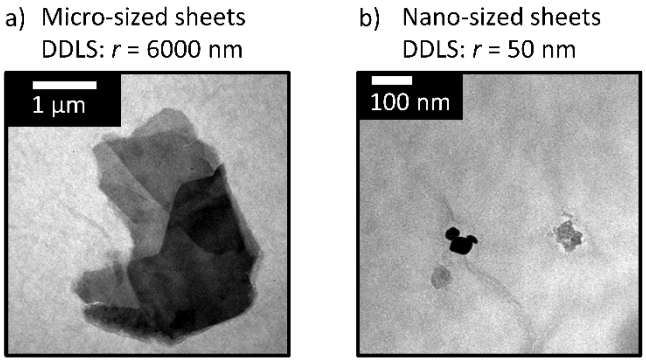

Fig. S4: TEM images of dried GO suspensions, which contain GO sheets with a mean lateral hydrodynamic radius of a) *r* = 6000 nm and b) *r* = 50 nm.

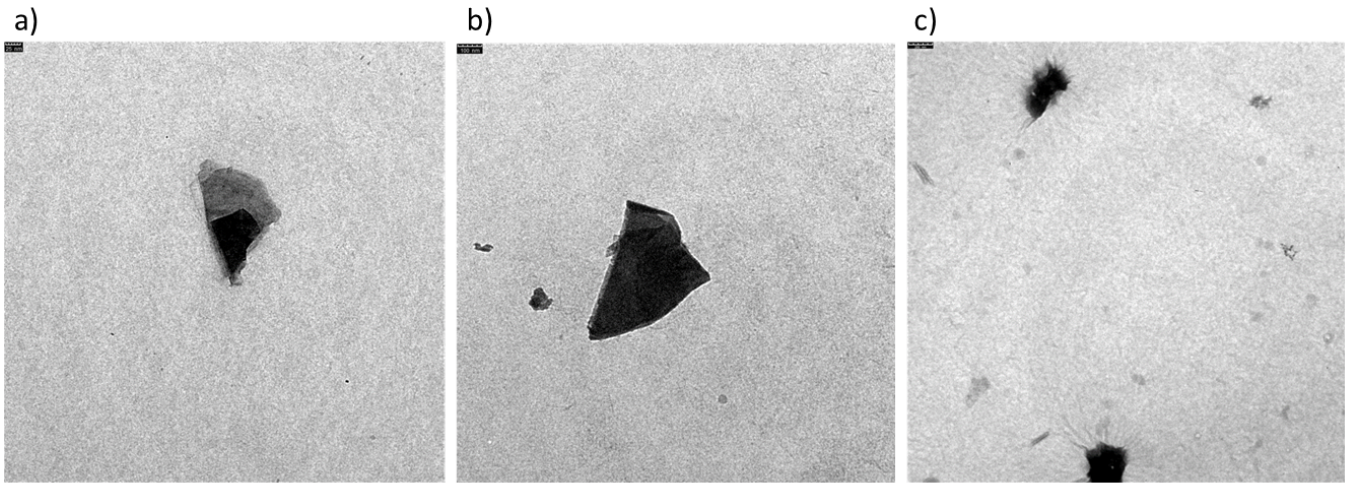

Fig. S5: TEM images of some GO sheets of a dried isotropic GO dispersion prepared by the oxidative exfoliation of graphite followed by sonication. There are a) irregular shaped and aggregated (scale bar 25 nm) and b) folded GO sheets (scale bar 100 nm). c) Overview image of some GO sheets (scale bar 250 nm). Due to the non-circular lateral shape of some sheets, the sheet diameter was obtained by averaging the size of the longest and the smallest diameter.

ESI 5: Influence on a non-infinite thin thickness

The influence of a non-infinite thin thickness was considered by comparing the model for circular, infinite thin disks with a model for oblate spheroids using different sheet thicknesses and the Stokes-Einstein model for spherical particles.

Oblate spheroid model:[1–3]
Aspect ratio:

$$\rho = d/t,$$

with the sheet diameter d and the thickness t.
Translational diffusion coefficient:

$$D_t = \frac{k_B T \cdot G(\rho)}{6\pi\eta r},$$

with the Boltzmann constant k_B, the temperature T, the viscosity η, the sheet radius from the translational diffusion r_t coefficient and:

$$G(\rho) = \frac{\arctan\left(\sqrt{\rho^2-1}\right)}{\sqrt{\rho^2-1}}.$$

The influence of a non-infinite thickness is small, because the change of D_t with t is very low for small thicknesses t < 50 nm and also negligible low for higher thicknesses of t > 50 nm. The spherical model could be used as a rough approximation to obtain the hydrodynamic radii.

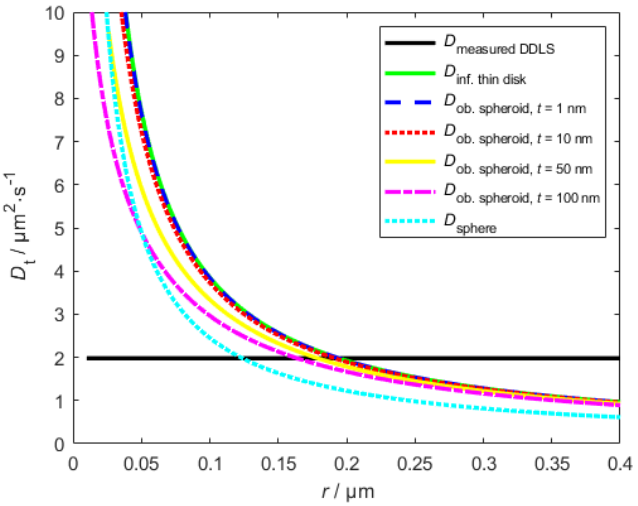

Fig. S6: Numeric calculation of the translational diffusion coefficients D_t of the GO sheets plotted against the hydrodynamic radius r under the assumption of a model for the diffusion of an oblate spheroid with different thickness of t = 1 nm, t = 10 nm, t = 50 nm and t = 100 nm compared to the model for the diffusion of an infinites thin disk and a sphere and to the measured diffusion coefficient $D_{measured\ DDLS}$. The calculated r is obtained from the intersect of $D_{measured\ DDLS}$ with D of the corresponding model.

ESI 6: Dynamic light scattering data for the fractions obtained with the size fractionation protocol

Values for D_T, D_R and $r(D_R)$ are shown in Tab. S1. The correlations functions $g_{2,VH}$-1, $g_{1,VH}$, as well as the inverse relaxation rates $\Gamma_{VH}(q^2)$ and the stretching exponents $\beta_{VH}(q)$ are depicted in the Fig. S6-9, for the fractions obtained with the fractionation protocol. With each fractionation step, clear trends are observed, namely that the nematic fraction contain the largest sheets, the biphasic medium-sized and the isotropic the smallest. The stretching factor is in general higher for the fractions compared to the initial sample before fractionation, indicating a lower polydispersity after fractionation. Further, however not for all scattering vectors the stretching factor and so the polydispersity is larger in the nematic fractions than in the biphasic and in the isotropic fraction. Additionally, the stretching factor decrease with the scattering vector for all sample. For some very monodisperse samples at low scattering vectors, a stretching factor higher than 1 was found. This error could result from a slightly ordering of the GO sheets, due to errors in the normalization or fitting process or due to convective motion due to a temperature gradient caused by the local heating of the laser beam.[4] But this error seems to contribute to all samples in a systematic way and so we can use the stretching factors as a relative measure of the polydispersity. In principle, the observed trends in sheet size and polydispersity are seen for almost all scattering vectors, but it was observed that with increasing scattering vector the scattering intensity decreased, which results in an increased error for larger scattering vectors. Therefore, for the comparison of the different fractions a scattering vector of q = 6.46 µm^{-1} was used.

The sheet size distribution has a strong effect on the rotational diffusion coefficient. So, the mean lateral hydrodynamic radius from the rotational diffusion coefficient was calculated to $r_{1(I+N)\,2(I+N)}$ = 1.2 µm for a rather monodisperse fraction and is therefore in the same order of magnitude as the radius determined from the translational diffusion coefficient. For polydisperse samples with β < 0.9 at q = 6.46 µm^{-1} both values differ by a factor of 2-12 and for the less polydisperse fractions with β ≥ 0.9 at q = 6.46 µm^{-1} by a factor of 2-5 (see Tab. 1 and Tab. S1).

Tab. S1: Translational D_t and rotational D_r diffusion coefficients as well as the average lateral hydrodynamic radii determined from the rotational diffusion coefficient $r(D_R)$ for the different fractions obtained after the first and second fractionation step, as well as from the samples before fractionation.

	fraction	D_t / µm^{2}s^{-1}	D_r / s^{-1}	r (D_r) / nm
before fract.		0.067	0.035	2.3
fractionation step 1	1I	0.11	0.11	1.6
	1I+N	0.10	0.13	1.5
	1N	0.042	0.29	1.1
fractionation step 2 of 1I	1I2I	0.18	0.0048	4.4
	1I2I+N	0.082	0.056	1.9
	1I2N	0.044	0.33	1.1
fractionation step 2 of 1(I+N)	1I+N2I	0.15	0.039	2.2
	1I+N2I+N	0.12	0.24	1.2
	1I+N2N	0.067	0.39	1.0
fractionation step 2 of 1N	1N2I	0.095	0.098	1.6
	1N2I+N	0.057	0.21	1.2
	1N2N	0.029	0.45	1.0

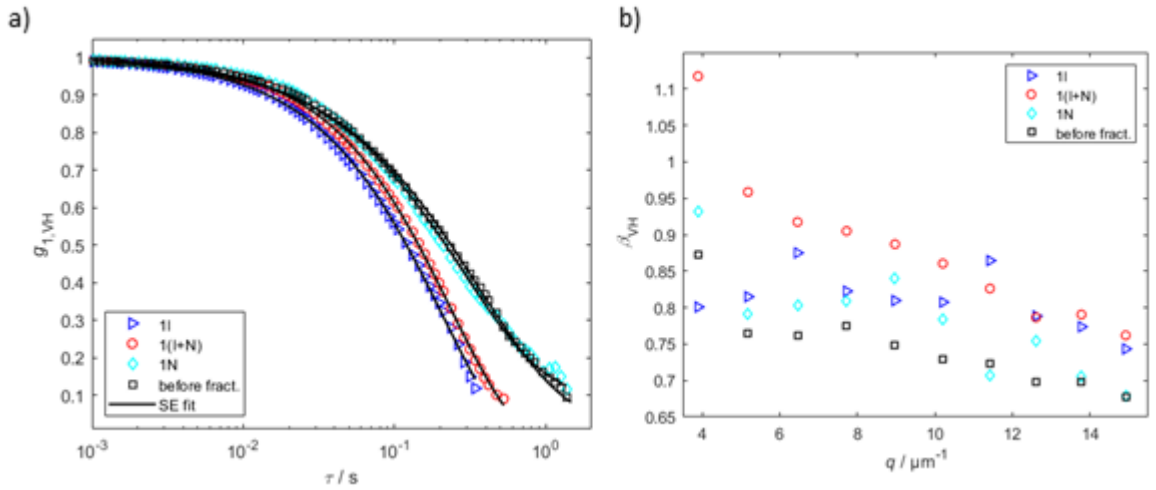

Fig. S7: a) Amplitude correlation functions $g_{1,VH}$, stretched single exponential (SE) fit at a scattering vector of q = 6.46 µm^{-1} and b) stretching exponent β_{VH} in VH geometry for the fractions 1I (isotropic fraction), 1(I+N) (biphasic fraction) and 1N (nematic fraction) measured after the first fractionation step and compared to the sample before fractionation.

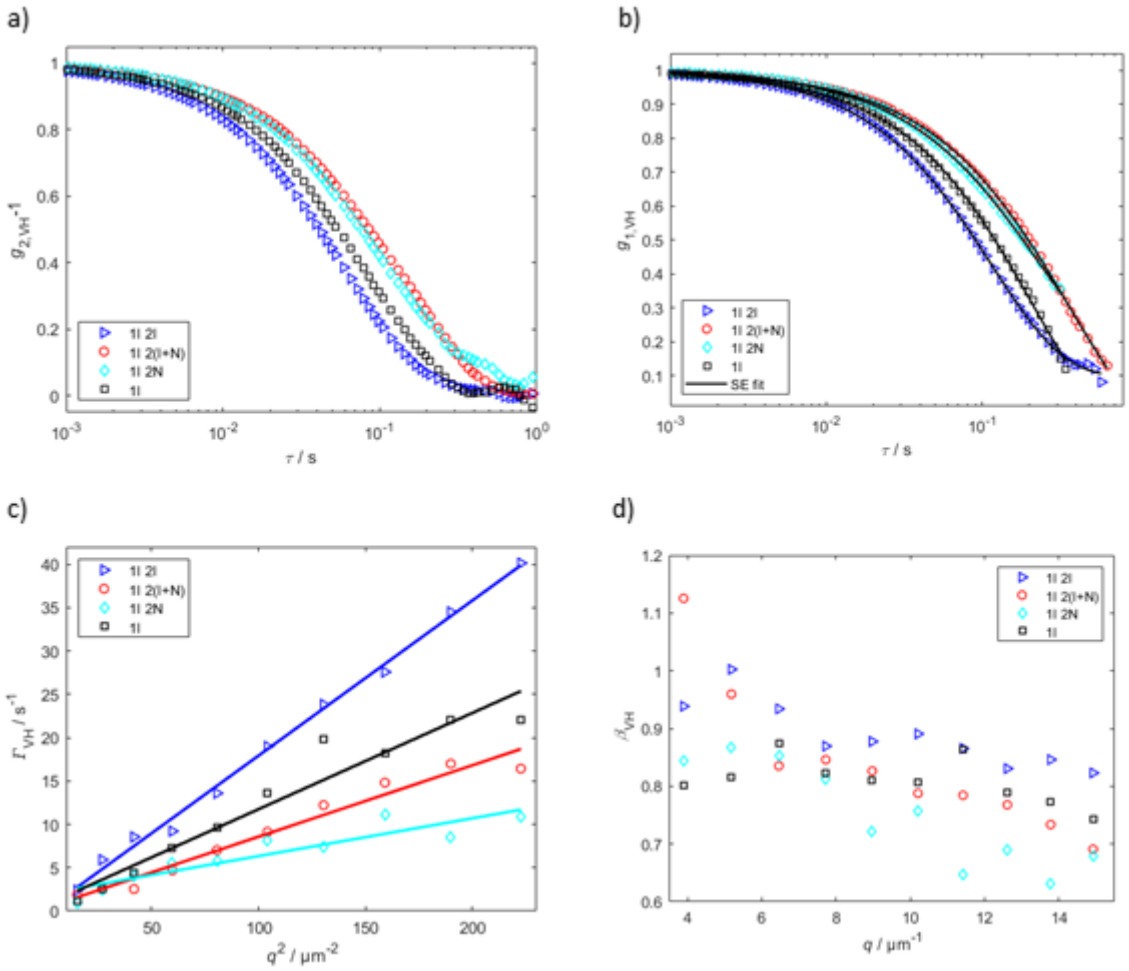

Fig. S8: a) **I**ntensity correlation functions $g_{2,VH}$-1, b) amplitude correlation functions $g_{1,VH}$, stretched single exponential (SE) fit at a scattering vector of q = 6.46 µm^{-1}, c) mean inverse relaxation time Γ_{VH} and d) stretching exponent β_{VH} in VH geometry for the fractions 1I (isotropic fraction) after the first fractionation step and the fractions 1I 2I, 1I 2(I+N) and 1I 2N measured after the second fractionation step.

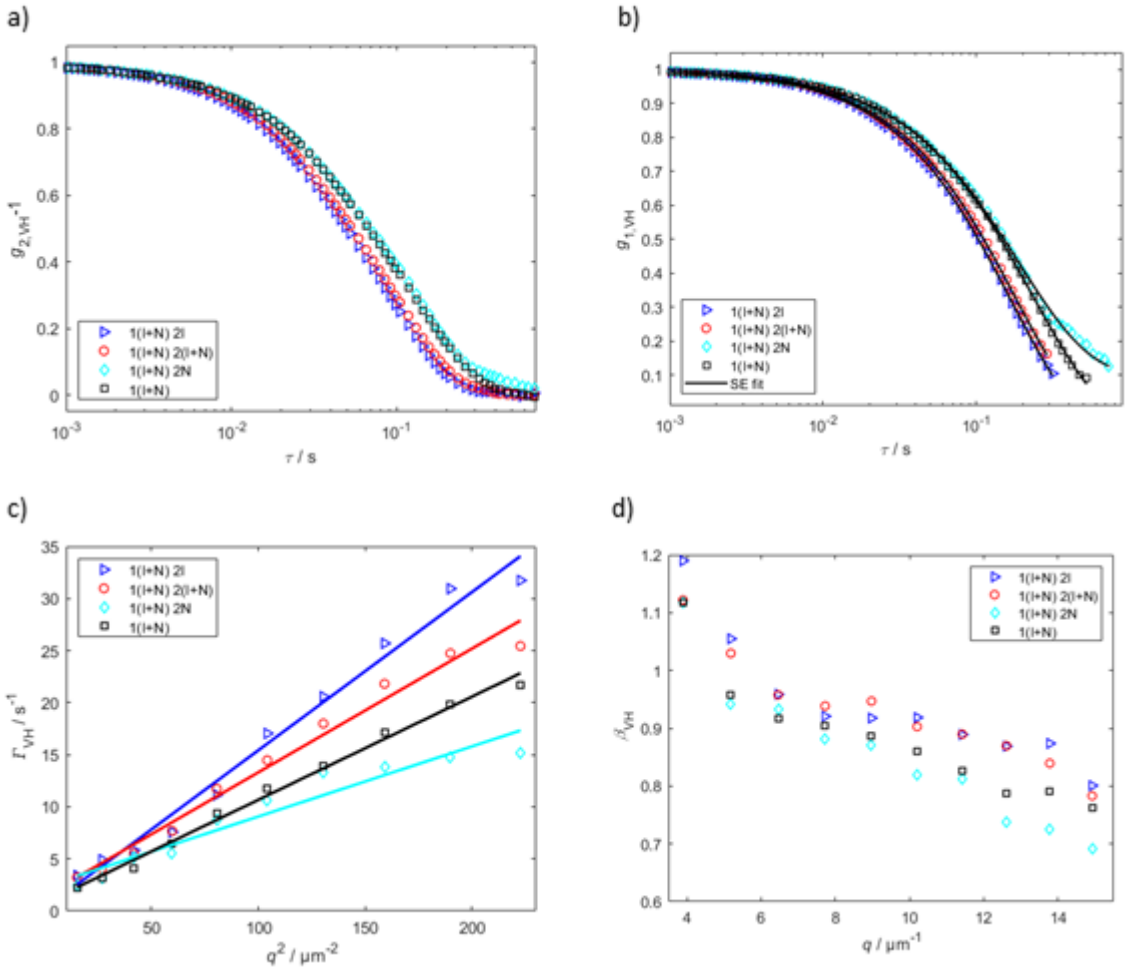

Fig. S9: a a) **I**ntensity correlation functions $g_{2,VH}$-1, b) amplitude correlation functions $g_{1,VH}$, stretched single exponential (SE) fit at a scattering vector of q = 6.46 µm^{-1}, c) mean inverse relaxation time Γ_{VH} and d) stretching exponent β_{VH} in VH geometry for the fractions 1(I+N) (biphasic fraction) after the first fractionation step and the fractions 1(I+N) 2I, 1(I+N) (2I+N) and 1(I+N) 2N measured after the second fractionation step.

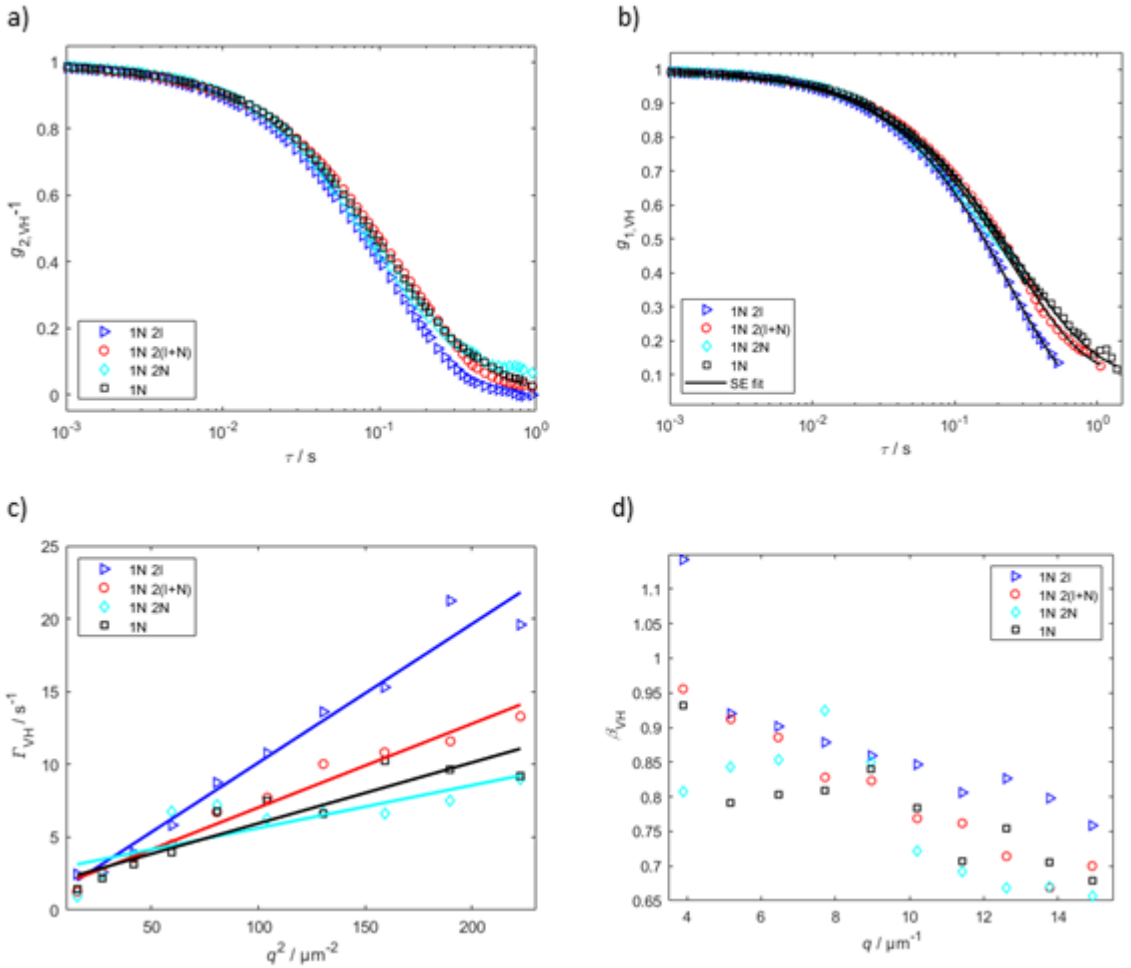

Fig. S10: a) **I**ntensity correlation functions $g_{2,VH}$-1, b) amplitude correlation functions $g_{1,VH}$, stretched single exponential (SE) fit at a scattering vector of q = 6.46 µm^{-1}, c) mean inverse relaxation time Γ_{VH} and d) stretching exponent β_{VH} in VH geometry for the fractions 1N (nematic fraction) after the first fractionation step and the fractions 1N 2I, 1N (2I+N) and 1N 2N measured after the second fractionation step.

References

[1] R. Vasanthi, S. Bhattacharyya, B. Bagchi, *J. Chem. Phys.* 2002, **116**, 1092–1096.

[2] H. Shimizu, *J. Chem. Phys.* 1962, **37**, 765–778.

[3] E. Smith, Experiments in Light Scattering : Examining Aqueous Suspensions of Graphene Oxide and the Aggregation Behavior of Bordeaux Dye, Swartmore College, 2010.

[4] O. D. Parashchuk, T. V. Laptinskaya, M. S. Ananieva, D. Y. Paraschuk, *Soft Matter* 2011, **7**, 5585–5594.

